small structures
www.small-structures.com

Discovery of Molecular Intermediates and Nonclassical Nanoparticle Formation Mechanisms by Liquid Phase Electron Microscopy and Reaction Throughput Analysis

Jiayue Sun, Birk Fritsch, Andreas Körner, Mehran Taherkhani, Chiwoo Park, Mei Wang, Andreas Hutzler, and Taylor J. Woehl**

Formation kinetics of metal nanoparticles are generally described *via* mass transport and thermodynamics-based models, such as diffusion-limited growth and classical nucleation theory (CNT). However, metal monomers are commonly assumed as precursors, leaving the identity of molecular intermediates and their contribution to nanoparticle formation unclear. Herein, liquid phase transmission electron microscopy (LPTEM) and reaction kinetic modeling are utilized to establish the nucleation and growth mechanisms and discover molecular intermediates during silver nanoparticle formation. Quantitative LPTEM measurements show that their nucleation rate decreases while growth rate is nearly invariant with electron dose rate. Reaction kinetic simulations show that Ag_4 and Ag^- follow a statistically similar dose rate dependence as the experimentally determined growth rate. We show that experimental growth rates are consistent with diffusion-limited growth *via* the attachment of these species to nanoparticles. The dose rate dependence of nucleation rate is inconsistent with CNT. A reaction-limited nucleation mechanism is proposed and it is demonstrated that experimental nucleation kinetics are consistent with Ag_4^{2+} aggregation rates at millisecond time scales. Reaction throughput analysis of the kinetic simulations uncovered formation and decay pathways mediating intermediate concentrations. We demonstrate the power of quantitative LPTEM combined with kinetic modeling for establishing nanoparticle formation mechanisms and principal intermediates.

1. Introduction

Metal nanoparticles are commonly utilized as heterogeneous catalysts, electrocatalysts, and in optical materials.[1–4] Nanoparticle functional properties derive from their surface and atomic structure, composition, and morphology. The prevailing synthesis methods involve the chemical reduction of inorganic metal salt precursors with organic ligands to form colloidal metal nanoparticles. While the colloidal synthesis method is relatively simple in practice, the underlying nanochemistry continues to perplex and fascinate researchers.[5–7] Structure–processing–function relationships for colloidal nanoparticles remain elusive due in large part to incomplete understanding of the physicochemical processes underlying their formation. Rational control over nanoparticle characteristics, and thus their functional properties, requires uncovering the complex nanochemistry involved in their formation.

Mechanisms of colloidal metal nanoparticle formation typically invoke nucleation and monomer attachment-based growth models.[8–11] Classical nucleation theory

J. Sun
Department of Chemistry & Biochemistry
University of Maryland
College Park, MD 20742, USA

B. Fritsch, A. Körner, A. Hutzler
Helmholtz Institute Erlangen-Nürnberg for Renewable Energy (IET-2)
Forschungszentrum Jülich GmbH
Cauerstraße 1, Erlangen 91058, Germany
E-mail: a.hutzler@fz-juelich.de

The ORCID identification number(s) for the author(s) of this article can be found under https://doi.org/10.1002/sstr.202400146.

DOI: 10.1002/sstr.202400146

A. Körner
Department Chemical and Biological Engineering
Friedrich-Alexander-Universität Erlangen-Nürnberg
Immerwahrstraße 2a, 91058 Erlangen, Germany

M. Taherkhani
Electron Devices (LEB)
Friedrich-Alexander-Universität Erlangen-Nürnberg
Cauerstraße 6, 91058 Erlangen, Germany

C. Park
Department of Industrial and Systems Engineering
University of Washington
Seattle, WA 98195, USA

M. Wang, T. J. Woehl
Department of Chemical and Biomolecular Engineering
University of Maryland
College Park, MD 20742, USA
E-mail: tjwoehl@umd.edu

(CNT) describes the formation of crystalline nanoparticle seeds from insoluble metal atoms generated by chemical reduction of metal precursors.[8,12] After nucleation ceases due to a decrease in supersaturation ratio,[9] diffusion and attachment of monomers to the nuclei is thought to cause growth.[13,14] However, a growing body of evidence suggests that colloidal nanoparticles form by nonclassical nucleation and growth mechanisms. Several mechanisms have been proposed,[8,15] such as continuous nucleation and autocatalytic growth (the Finke–Watzke mechanism),[16–18] prenucleation clusters,[19,20] phase separation,[7,21] oriented attachment,[22–24] and aggregative growth.[25–28] Indeed, these mechanisms are expected based on the large thermodynamic driving force for precipitation of solid metal nanoparticles, which indicates the nucleation-free energy barrier will be exceedingly small.[29] In this case, reaction kinetics and diffusion of precursors will be the primary factors kinetically limiting particle formation. The formation mechanism is expected to depend on the specific chemistry of the synthesis,[30] including the metal(s), solvent,[31] organic ligand,[32–34] chemical reductant,[35] and temperature. Thus, kinetic measurements coupled with chemical analysis and modeling are required to elucidate the formation mechanisms and nanochemistry of metal nanoparticle synthesis on a case-by-case basis.

Direct evidence from in situ small angle X-ray scattering (SAXS) and liquid phase transmission electron microscopy (LPTEM) has discovered and substantiated nonclassical nanoparticle formation mechanisms.[25,27,28,32,36,37] However, in situ LPTEM and SAXS do not provide information about the chemical identity of intermediate species or chemical reactions controlling nanoparticle nucleation and growth. LPTEM enables direct imaging of nanoparticle morphology in a liquid environment with atomic to nanometer-scale spatial resolution. Many LPTEM studies have been dedicated to elucidating the nucleation and growth mechanisms of nanoparticles.[21,38–41] The vast majority of these studies have utilized electron beam radiolysis to create chemical radicals that reduce metal ion precursors to metal nanoparticles.[42,43] However, radiolysis generates both reducing and oxidizing radicals in a complex network of nearly ≈100 reactions for pure water,[44] indicating both metal oxidation and reduction reactions can be active. Graphene liquid cell (GLC) LPTEM imaging enables direct atomic resolution imaging in liquid, which has revealed cluster-aggregation and coalescence-based formation of metal nanoparticles.[28,28,45] Systematically varying reaction conditions during GLC-based LPTEM imaging remains challenging due to the short lifetime of GLCs[46] and the lack of fluid flow. Despite these challenges, recent work has demonstrated systematic control over metal nanoparticle etching kinetics.[47,48] In contrast, microelectromechanical systems- (MEMS-) based LPTEM imaging utilizes electron transparent dielectric films to contain thicker liquid films (hundreds of nm) and thus have lower spatial resolution (≈1 nm). These methods uniquely enable control over temperature, precursor composition, and fluid flow.[49] MEMS-based LPTEM imaging together with radiolysis kinetic simulations[44,50–52] and environmental control has enabled quantitatively measuring the effect of precursor reaction kinetics on nanoparticle formation kinetics.[38,50,53–59] However, LPTEM imaging provides limited chemical information during nanoparticle formation reactions. Real-time high angle annular dark field imaging reveals differences in atomic number during the formation of bimetallic and core-shell metal nanoparticles.[28,60] Nevertheless, direct chemical analysis with energy-dispersive X-ray spectroscopy and electron energy loss spectroscopy mapping cannot probe chemistry in real time due to slow acquisition time and low signal-to-noise ratio.[61,62] LPTEM imaging cannot identify molecular scale intermediates or determine the composition of multimetallic nanoparticles or clusters in real time. As correlative analytical methods like mass spectrometry for detecting molecular species are unavailable, radiolysis simulations have emerged as powerful tools to unveil the solution chemistry during LPTEM. However, thus far those simulations have typically only considered solvent radiolysis and excluded intermediate metal species.

Aqueous silver nitrate solutions form stable metal clusters and ions in response to high-energy ionizing radiation, which are thought to be intermediate species to silver nanoparticles.[63–66] Prior work on silver nanoparticle formation mechanisms has focused either on the physical nucleation and growth mechanisms (e.g., LPTEM or in situ SAXS) or on silver cluster species (e.g., pulse radiolysis experiments). *This has left a gap in understanding which molecular intermediate species contribute to nucleation and growth processes*. Advances in quantitative measurement of nanoparticle formation kinetics with LPTEM[42,56,67] and numerical modeling of the radiolysis kinetics of aqueous metal precursors[50,59,68,69] present a unique opportunity to address this knowledge gap. In this article, we utilize quantitative LPTEM measurements of silver nanoparticle nucleation and growth kinetics and a reaction kinetic model to uncover the physical mechanisms involved in radiolytic silver nanoparticle nucleation and growth and the underlying reaction intermediates. This work interprets nanoparticle formation kinetics in terms of large-scale reaction network simulations (200 reactions, 49 species) that provide time- and dose rate-dependent silver ion and cluster concentrations. Fitting quantitative nucleation and growth models to LPTEM data, comparison to trends in the silver reaction kinetic model, and scaling analysis indicated Ag^- and Ag_4 were the intermediate species causing the growth of silver nanoparticles *via* diffusion-limited attachment. We rigorously establish that nucleation kinetics are inconsistent with CNT and are instead consistent with reaction rate-limited aggregation of transient Ag_4^{2+} clusters. We introduce a reaction throughput analysis to uncover the chemical pathways for formation of the principal intermediate species. While most prior works have interpreted nanoparticle nucleation and growth kinetics based on steady-state product concentrations, this work emphasizes the importance of considering transient populations of reaction products to interpret nucleation mechanisms. While LPTEM synthesis conditions differ from traditional solution chemistry,[43] prior work has shown that LPTEM experiments maintain similar conditions as bulk synthesis using a strong chemical reducing agent like sodium borohydride.[32,37] This indicates that after considering the differences between electron beam synthesis and solution chemistry, insights from this work are expected to inform more rational synthesis of nanoparticles *via* control of reaction intermediates. The ever-increasing complexity of functional colloidal nanoparticles, such as high entropy alloys and oxides,[70] halide perovskites,[71] and heterostructured nanoparticles,[72] make it critical to understand and rationally control reaction intermediates to tailor nanoparticle characteristics.[20]

This work demonstrates that a combination of chemical reaction network analysis and quantitative LPTEM imaging can uncover physical mechanisms of nanoparticle formation, intermediate species, and chemical pathways underlying the formation and decay of intermediates.

2. Results and Discussion

Radiolysis of water with 200 keV TEM beam electrons generates strongly reducing radicals that reduce aqueous silver ions to silver nanoparticles.[38,44] The radiolysis of deaerated aqueous silver nitrate (0.1 mM) in 100 mM *tert*-butanol was simulated using a time-dependent homogeneous reaction kinetic simulation method as described in prior work (**Figure 1**, see Experimental Section for details).[44,50,54,56,73–76] The simulation included reactions for pure water, nitrate ions, silver cations, silver clusters, and *tert*-butanol (Table S1 and Figure S1, Supporting Information).[56,63,64,73–75,77–85] In particular, the silver radiolysis reaction set, which has been extensively studied in the radiation chemistry field, included several Ag oxidation states ranging from −1 to +3 and long-lived silver cluster species, e.g., Ag_2, Ag_4, and Ag_4^{2+}. Radiolysis species are assumed to be generated only from water radiolysis and the resulting species recombine and react with each other and the solutes. The simulations were performed for a range of electron dose rates, i.e., the amount of energy absorbed by the liquid sample from the electron beam, covering the experimental parameter space. Dose rates are presented in terms of absorbed power [$1\,W\,kg^{-1} = 1\,J\,(kg\,s)^{-1} = 1\,Gy\,s^{-1}$]. We used radical generation values (*G*-values) for pure water from Hill and Smith for 200 keV electrons (Table S2, Supporting Information).[44,86] Figure 1a shows the time-dependent concentration of all the silver species at a dose rate of $1\,MGy\,s^{-1}$ (see Figure S2, Supporting Information for concentrations at other dose rates). Wide variations in concentrations were noted between different silver species and for the same species over time. Importantly the concentration of all simulated species eventually reached a steady state at a time that depended on the dose rate. This indicates the simulation obeyed mass and charge balance and that each species involved has at least one generation and one decay pathway. Figure 1b shows the steady state silver species concentrations as a function of dose rate over the range utilized experimentally. Schneider et al. showed that the steady-state concentration of radiolysis species roughly followed a power law dependence on the dose rate:[44]

$$c_i^{ss}(\dot{d}) = \alpha_i \dot{d}^{\beta_i} \quad (1)$$

Here, $c_i^{ss}(\dot{d})$ is the dose rate-dependent steady-state concentration of each silver species, *i*, $\dot{d}$ is the dose rate, and α_i and β_i are fitted constants. We fit Equation (1) to the steady-state concentrations in Figure 1b (lines) to obtain α_i and β_i for each silver species (**Table 1**).

Interestingly, the model showed that the silver cluster species, Ag_4, had the largest steady-state concentration. We note that while larger clusters certainly form during radiolysis of $AgNO_3$,[65] rate constants and reactions are only reported for clusters as large as Ag_4. The stability of the Ag_4 cluster is counter to prior measurements at lower dose rates, which showed that Ag_4 clusters underwent rapid oxidation by dissolved O_2 to form Ag_4^{2+}.[65,66] Here, we assumed that Ag_4 clusters underwent oxidation by dissolved O_2 following the same kinetics as silver monomers, as there was no kinetic data available for this reaction (see below). These samples were sparged with argon to remove O_2 and the high dose rates applied continuously to the image

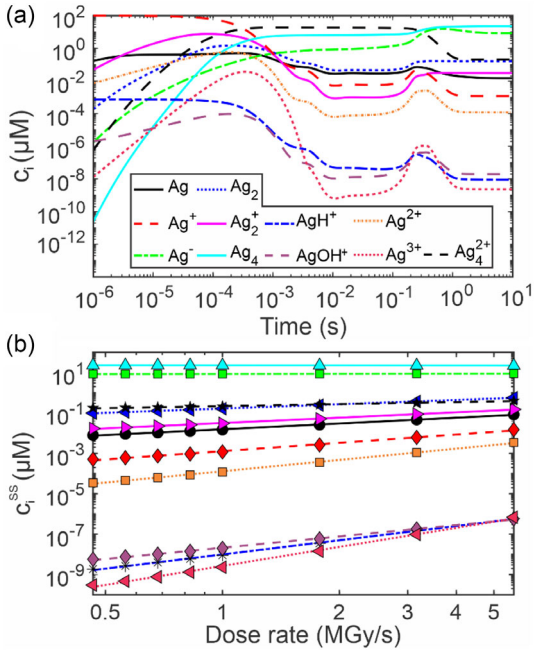

Figure 1. Aqueous silver nitrate radiolysis simulations. The silver nitrate concentration was 0.1 mM, the *tert*-butanol concentration was 100 mM, and the electron energy was 200 keV. a) The concentration of silver species as a function of time for a dose rate of 1 MGy s^{-1}. b) Steady-state concentration of silver species as a function of dose rate. The data points are from the simulation and the solid lines are power law fits of the form shown in Equation (1).

Table 1. Power law coefficients for fitting of the steady-state silver species concentrations. β_i represents the rate of increase or decrease with dose rate, while α_i represents the relative concentration of the species. The errors represent plus or minus the standard error associated with the least squares fit.

Species	α_i [μM]	β_i
Ag	154.12721 ± 0.00022	0.951 ± 0.017
Ag^+	$(127.5 \pm 3.8) \times 10^{-5}$	1.367 ± 0.036
Ag^-	8.430 ± 0.020	0.0139 ± 0.0027
Ag_2	0.1640 ± 0.0010	0.7059 ± 0.0074
Ag_2^+	0.03148 ± 0.00041	0.878 ± 0.016
Ag_4	22.547 ± 0.023	-0.0108 ± 0.0012
Ag_4^{2+}	0.2159 ± 0.0028	0.334 ± 0.015
AgH^+	$(9.91 \pm 0.31) \times 10^{-9}$	2.337 ± 0.038
$AgOH^+$	$(2.138 \pm 0.054) \times 10^{-8}$	1.859 ± 0.032
Ag^{2+}	$(1.297 \pm 0.035) \times 10^{-4}$	1.855 ± 0.032
Ag^{3+}	$(2.68 \pm 0.14) \times 10^{-9}$	3.129 ± 0.062

region generated hydrated electrons that rapidly converted any radiolytically formed O_2 to superoxide (O_2^-) radicals. Additionally, a high Ag^- concentration was observed. Prior work showed that zero-valent silver rapidly absorbed electrons from superoxide radicals to generate negatively charged silver monomers and nanoparticles.[84,87] The high steady-state concentration of Ag^- is likely due to eventual depletion of Ag^+, which is the main species consuming Ag^- (Table S1, Supporting Information).[84,87] The growth rate of nanoparticles *via* the diffusion-limited growth mechanism, i.e., monomer attachment, is directly proportional to the precursor concentration.[14] If this mechanism explains nanoparticle growth here, the kinetic simulations suggest that Ag_4 and Ag^- contribute most significantly to nanoparticle growth. Interestingly, the steady state Ag_4 and Ag^- concentrations were nearly *invariant with dose rate*. This contrasts with silver monomers and other silver clusters, whose steady concentration increased with dose rate.

2.1. Data Fitting-Based Discovery of Nanoparticle Formation Mechanisms and Reaction Intermediates

Silver clusters have been experimentally shown to form from silver nitrate solutions under pulse radiolysis conditions in several prior works discussed above, which together with kinetic modeling indicates they are expected to be present in the experiments described here. While it is possible to detect the presence of silver clusters with optical or mass spectrometry,[88,89] the sample volumes and predicted cluster concentrations for these experiments are far below the requirements for these methods. Instead, we utilized a data fitting-based approach using experimental silver nanoparticle nucleation and growth rates as a function of dose rate[56] to establish the important cluster intermediates. We utilized nucleation and growth rate values from this dataset, with at least two measurements taken for each rate at each of the three dose rates. Briefly, the dose rate was varied by changing the scanning TEM (STEM) probe spot size, i.e., the beam current, at a constant magnification of 100 kX (see Experimental Section). Dose rate-controlled LPTEM measurements of silver nanoparticle nucleation rate (J) and growth rate ($\mathrm{d}r/\mathrm{d}t$) were directly fit to mathematical models using the following approach. We tested several nucleation and growth models against the experimental formation kinetics, each of which expressed nucleation or growth rate as a function of silver concentration, material properties, and universal constants. The silver species contributing to nucleation and growth was taken as unknown and determined by data fitting. We first recast the concentration term in each nucleation and growth model in terms of the dose rate using the power law function shown in Equation (1). This enabled directly fitting models to the dose rate dependent nucleation and growth rates while taking the power law coefficients, α and β, and groupings of material constants and universal constants as fitting parameters. The fitted values of the material and universal constants were then compared to theoretical estimates to assess the compatibility of the model. If the material constants were reasonable then the model was considered potentially consistent with the kinetic data; if they were not consistent then we ruled out the model. The fitted power law coefficients were then compared to α_i and β_i of each silver species from the numerical reaction simulation (Table 1) to identify which intermediate species contributed to nucleation and growth. The experimental data from LPTEM is relatively noisy, which is due to experiment-to-experiment variability in precursor concentration and carbon contamination.[56] We refer readers to the original experimental work by Wang et al. which provides a discussion on reproducibility.[56] We carefully considered statistics in this study and reported the confidence interval and standard error of all power law fits and fitting parameters throughout the article.

2.2. Establishing the Nanoparticle Growth Mechanism

Ostwald ripening describes colloidal metal nanoparticle growth *via* diffusion of low solubility metal species to the nanoparticle surface where they attach *via* a surface reaction. The Lifshitz–Slyozov–Wagner (LSW) model expresses the growth rate $\left(\frac{\mathrm{d}r}{\mathrm{d}t}\right)$ of spherical particles in a liquid solution as:[90,91]

$$\frac{\mathrm{d}r}{\mathrm{d}t} = \frac{2\sigma V_\mathrm{m}^2 c\left(\frac{r}{r_\mathrm{b}} - 1\right)}{RTr\left[D^{-1} + \left(k_\mathrm{d} r\right)^{-1}\right]} \tag{2}$$

Here, r is the particle radius, t is time, σ is the nanoparticle surface energy, V_m is the molar volume of the nanoparticle, c is the bulk concentration of the silver precursor, r_b is the critical nuclei radius, R is the universal gas constant, T is temperature, D is the diffusion coefficient of the silver precursor, and k_d is the surface attachment rate constant. Assuming that the surface reaction rate is much larger than the characteristic diffusion rate, the growth is diffusion limited and Equation (2) reduces to:

$$\frac{\mathrm{d}r}{\mathrm{d}t} \approx Kcr^{-2} \tag{3}$$

where $K = \frac{2\sigma D V_\mathrm{m}^2}{RT}\left(\frac{r}{r_\mathrm{b}} - 1\right)$. Assuming the silver precursor concentration is constant with time and follows a power law dependence on dose rate as in the reaction simulations, $c = \alpha' \dot{d}^{\beta'}$, yields an expression that can be directly fit to experimental growth rates measured as a function of dose rate:

$$\frac{\mathrm{d}r}{\mathrm{d}t} r^2 = K\alpha' \dot{d}^{\beta'} \tag{4}$$

Here, the terms on the left-hand side of the expression were determined experimentally for three dose rates from a precursor solution identical to that in the simulation. **Figure 2**a shows an exemplary series of time-lapsed images taken with LPTEM showing the nucleation and growth of silver nanoparticles over a time of 30 s. High-resolution TEM (HRTEM) characterization of the silver nanoparticles can be found in the prior work by Wang et al.[56] The growth rate and average size of each nanoparticle over this time, r, was determined by image analysis and averaged across all nanoparticles at each dose rate to yield the data points in Figure 2b (see Figure S3, Supporting Information and Experimental Section for additional details). The silver species contributing to nanoparticle growth are unknown so the coefficients $K\alpha'$ and β' were taken as fitting parameters when fitting Equation (4) to the experimental growth rate data.

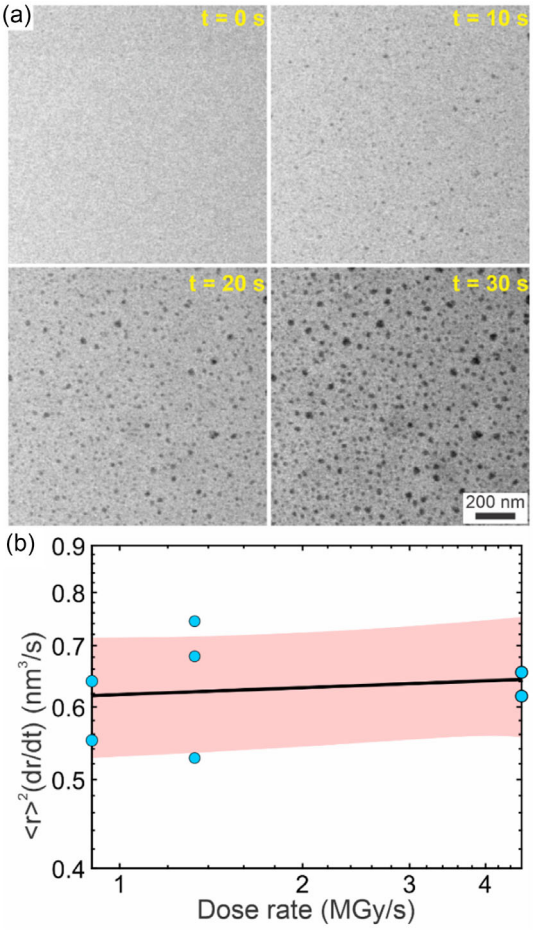

Figure 2. LPTEM images of nanoparticle growth and fitting the LSW model to the growth rate. a) Time-lapsed LPTEM images showing nucleation and growth of silver nanoparticles. b) Average nanoparticle growth rate multiplied by average radius, r, squared as a function of dose rate (blue circles). The black line is a power law fit according to Equation (4) with fitting parameters of $\beta' = 0.025 \pm 0.075$ and $K\alpha' = 0.62 \pm 0.06 \frac{\text{nm}^3}{\text{s}}$. The red-shaded region represents the 95% confidence interval of the fit.

Linear least squares fitting of Equation (4) to the experimental growth rates yielded values of $\beta' = 0.025 \pm 0.075$ and $K\alpha' = 0.62 \pm 0.06 \frac{\text{nm}^3}{\text{s}}$ (Figure 2b). The only silver species with power law coefficients within the margin of error of the fitted parameters were Ag_4 ($\beta_{Ag_4} = -0.0108 \pm 0.0012$) and Ag^- ($\beta_{Ag^-} = 0.0139 \pm 0.0027$). Likewise, Ag_4 and Ag^- had the highest steady-state concentrations. In addition to identifying the requisite silver precursors from the power law parameters, the fitted value of K must be consistent with known material properties and constants for this model to be viable. We assume a silver surface energy of $\sigma = 1\,\text{J m}^{-2}$,[92] silver cluster diffusion coefficient of $D \approx 10^{-9} \frac{m^2}{s}$, $\alpha' \approx 10\,\mu\text{M}$ (Table 1), and $\left(\frac{r}{r_b} - 1\right) \approx 1$. The latter parameter is approximately of order unity based on an estimated critical radius of $r_b \approx 0.5\,\text{nm}$[21,57] and an average radius of $r \approx 3\,\text{nm}$ (Figure S3, Supporting Information). These values yield a scaling estimate of $K\alpha' \approx 1000 \frac{\text{nm}^3}{\text{s}}$, which is 4–5 orders of magnitude larger than obtained by fitting. There could be several potential reasons for this discrepancy. Prior work has shown that diffusivity of solutes during LPTEM are often several orders of magnitude lower than in bulk liquid due to close association of solutes with the silicon nitride substrate[51] and increased viscosity near the surface.[93] Prior work by White et al. estimated that Pb^{2+} had a diffusivity of $\approx 10^{-11} \frac{\text{m}^2}{\text{s}}$ during LPTEM observations of electrochemical lead plating and attributed this low value to high local Pb^{2+} concentrations.[94] TEM imaging of single atoms in ionic liquid thin films measured diffusivities up to 7 orders of magnitude smaller than the bulk value.[95] Taking the diffusion coefficient as an unknown, we can use the fitted value of $K\alpha'$ to estimate a silver species diffusion coefficient of $D \approx 10^{-12} \frac{\text{m}^2}{\text{s}}$. Based on the prior work, this estimated diffusion coefficient is reasonable for the confined environment during LPTEM experiments. It is possible to directly measure the diffusion coefficient of the visible nanoparticles with LPTEM imaging,[96] which could potentially be extrapolated to small clusters using the Stokes–Einstein expression. However, the final nanoparticles formed here were fixed to the silicon nitride substrate so their diffusion coefficient cannot be measured. Likewise, nanoparticle diffusion during LPTEM only follows Stokes–Einstein expression under limiting cases where the nanoparticles do not interact strongly with the substrate.[96,97] An additional explanation for the discrepancy between the fitted and theoretical value of K could be confinement effects during nanoparticle growth. The LSW model assumes noninteracting particles in a bulk fluid,[91] while nanoparticles formed very near each other in the experiments. Taken together, this analysis indicates the dose rate dependence of silver nanoparticle growth rate is consistent with diffusion-limited growth with Ag_4 and/or Ag^- species being the predominant intermediates.

2.3. Establishing the Nanoparticle Nucleation Mechanism

A similar approach was used to test whether the experimental nucleation rates were consistent with CNT. Briefly, CNT proposes that formation of a crystalline nanoparticle nuclei is kinetically limited by the energy penalty of generating new solid–liquid interfaces.[8] A sufficiently large nucleus is required to overcome the interfacial energy penalty, which yields a single free energy barrier to nucleation. The nucleation rate expression that emerges from CNT is:

$$\frac{dN}{dt} = J = A\exp\left[-f\frac{16\pi\gamma^3\nu^2}{3k_B^3T^3\ln^2(S)}\right] \quad (5)$$

Here, N is the number of particles per unit area, J is the nucleation rate, A is the Zeldovich factor, f is a shape factor accounting for the presence of a surface and nuclei shape, γ is the interfacial energy of a nucleus, ν is the atomic volume of silver, k_B is Boltzmann's constant, $S = \frac{c}{c_0}$ is the supersaturation ratio, c is the concentration of the nucleating silver species, and c_0 is the bulk solubility. As with the prior analysis, assuming the silver precursor concentration follows a power law dependence on dose rate, $c = \alpha''\dot{d}^{\beta''}$, yields a dose rate dependent expression for nucleation rate that can be fit to experimental data:

$$J = A\exp\left[-\frac{\chi}{\ln^2(\Gamma \dot{d}^{\beta''})}\right] \quad (6)$$

Here, A, $\chi = f\frac{16\pi\gamma^3\nu^2}{3k_B^3T^3}$, $\Gamma = \frac{\alpha''}{c_0}$, and β'' are taken as fitting parameters. The experimental nucleation rates were determined by dividing the total number of particles formed in each LPTEM movie by the total time of observation (Figure S3, Supporting Information). This method was used because the nucleation rate changed over time, prohibiting performing a linear fit. As with the growth rate, we determined the nucleation rate for at least two datasets for each of the three-dose rates. In contrast to the growth rate, nucleation rate clearly decreased as a function of increasing dose rate (**Figure 3**a). We fit the nucleation rate data with Equation (6) using nonlinear least squares fitting, which yielded values of $\chi = 18.6968 \pm 0.0007$, $\Gamma = 4.957 \pm 0.007$, and $\beta'' = -0.022 \pm 0.004$. Interpretation of this fit and the suitability of CNT to describe nucleation requires careful inspection of each fitting parameter value. The parameter χ represents a collection of material constants, the shape factor, and universal constants that are invariant with dose rate. Assuming an interfacial energy of $\gamma = 1\,\mathrm{J\,m^{-2}}$ and a shape factor range of $f = 0.1 - 1$ gives values of $\chi \approx 7000 - 70000$, two to three orders of magnitude larger than the experimental fitted value. An unrealistically low value of the interfacial energy or shape factor would be required to achieve the fitted value of χ. The parameter $\Gamma = \frac{\alpha''}{c_0}$ is related to the supersaturation ratio. The silver solubility is not well known but is thought to be on the order of $c_0 \approx 10^{-12}$ M.[21,57] A scaling estimate taking $\alpha'' \approx 10\,\mu$M yields a value of $\Gamma \approx 10^7$, which is six orders of magnitude larger than the value obtained by experimental fitting. An unrealistically high bulk solubility of silver ($c_0 \approx 10^{-5} - 10^{-6}$M) would be required to achieve the fitted value of Γ. Finally, the value of β'' is within a factor of two of β_{Ag_4} and β_{Ag^-} but outside the uncertainty bounds of these values (Table 1). Taken together, the unrealistic material constants from the data fitting and the disagreement of the fitted power law coefficient with the simulated silver species indicate the nucleation rate data are inconsistent with CNT. Given the prevalence of clusters formed during silver nitrate radiolysis, it is instead expected that the nucleation mechanism will involve cluster aggregation.

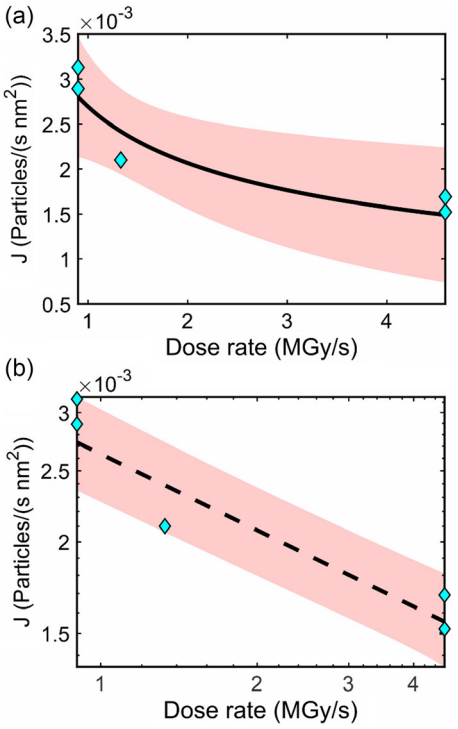

Figure 3. CNT and reaction-limited nucleation models are inconsistent with the experimental nucleation rates when considering steady-state concentrations of silver species. a) Nucleation rate as a function of dose rate at a magnification of 100 kX. The black line is a nonlinear least squares fit of CNT (Equation (6)). b) Nucleation rate as a function of dose rate on a log scale. The dashed black line is a nonlinear least squares fit of the reaction limited nucleation model (Equation (10)). The red-shaded regions in a,b) represent the 95% confidence interval of the fits.

A potential reason CNT was unable to describe the experimental data is that the supersaturation values are large here, on the order of 10^6–10^7. The fitting parameters from the fit in Figure 3b and CNT give an estimated critical nuclei radius of ≈1 Å, which is about the size of a single silver atom. This indicates a main assumption of CNT, that the nuclei are crystalline and have the properties of bulk silver, is invalid. Further, this indicates that particles will spontaneously grow from single atoms and that the interfacial energy penalty does not limit the phase transition kinetics.[29] In this case, the formation rate of reduced silver species is expected to be the limiting process controlling the effective nucleation rate of nanoparticles. Indeed, reaction kinetics has been invoked to explain nucleation mechanisms in cases where the precursor solubility is very small and the supersaturation ratio very large.[29] Here, we adopt a reaction-limited nucleation rate model derived by Xie et al.[29] which takes silver cluster aggregation as the rate-limiting step for particle nucleation:

$$2\,\mathrm{Ag}_i \xrightarrow{k} (\mathrm{Ag}_i)_2 \quad (7)$$

$$J \propto R_{(\mathrm{Ag}_i)_2} = k c_{\mathrm{Ag}_i}^2 \quad (8)$$

Here, $R_{(\mathrm{Ag}_i)_2}$ is the generation rate of $(\mathrm{Ag}_i)_2$ and k is the rate constant for the aggregation reaction. As with the prior analyses, inserting a power law expression for silver cluster concentration, $c_{\mathrm{Ag}_i} = \hat{\alpha}\dot{d}^{\hat{\beta}}$, yields:

$$J = \xi \dot{d}^{2\hat{\beta}} \quad (9)$$

where $\xi = k\hat{\alpha}^2$ is the product of the rate constant and square of the fitted power law prefactor, and $\hat{\beta}$ is the fitted power law exponent. Expressing Equation (9) in logarithmic format yields:

$$\ln(J) = \ln(\xi) + 2\hat{\beta}\ln(\dot{d}) \quad (10)$$

Equation (10) was fit to the experimental nucleation rate data taking ξ and $\hat{\beta}$ as fitting parameters, which yielded values of $\xi = 0.312 \pm 0.109$ and $\hat{\beta} = -0.173 \pm 0.073$ (Figure 3b). However, the fitted power law scaling exponent, $\hat{\beta}$, did not match any of the coefficients for the steady-state silver species concentrations (Table 1).

The experimental nucleation rate dependence on dose rate did not agree with CNT or reaction-limited aggregation. However, these analyses only considered the simulated steady-state concentrations of silver cluster species. Nucleation is a rapid transient process that could instead rely on *transient species concentrations*. The radiolysis simulations showed that several silver species, particularly Ag_4^{2+}, had the highest concentration of all species at millisecond time scales and then decayed to a steady-state concentration less than Ag_4 and Ag^- (cf. Figure 1a). Based on this observation, we hypothesized that elevated transient silver species concentrations mediated the nucleation kinetics. To test this hypothesis, we compared the power law dose rate dependence of several species concentrations as a function of reaction time to that determined by fitting the reaction-limited nucleation model (**Figure 4**).

We calculated the time-dependent power law dependence of concentration for three silver species with the highest concentrations, Ag_4^{2+}, Ag_4, and Ag^-. Figure 4a shows power law fits of the form, $c_i(t) = \alpha_i(t)\dot{d}^{\beta_i(t)}$, to each species concentration as a function of dose rate for reaction times of $t = 0.1$ ms, $t = 1$ ms, and $t = 10$ ms. We can see that except for Ag_4^{2+} at times between 1 and 10 ms, all species tested had a positive power law exponent, indicating their concentration increased with dose rate. Figure 4b shows the power law exponent, $\beta_i(t)$, for each species as a function of reaction time. Here, we see that Ag_4^{2+} has a negative power law exponent for times between 1 ms and 1 s, while Ag^- has a negative power law exponent between 1 and 5 s. Fitting the nucleation kinetics with the reaction-limited nucleation model yielded a power law dependence on dose rate of $\beta'' = -0.17 \pm 0.07$ (purple shaded region in the plot). Ag_4^{2+} showed negative power law exponents within this range between 1 and 10 ms with a peak concentration of 15–20 μM over this time range, which was greater than any other species. Ag^- showed a negative power law dependence on dose rate near a time of ≈1 s, but particles were already past the nucleation stage at this time and actively undergoing growth. This result suggests that Ag_4^{2+} aggregation is the rate-limiting step for nucleation. This conclusion is supported by scaling estimates for the collision time of two Ag_4^{2+} ions at a concentration of ≈10 μM. Here, the average interatomic separation of two Ag_4^{2+} ions is ≈30 nm (assuming a random spatial distribution of ions). Assuming diffusion limited kinetics for Ag_4^{2+} aggregation and a Ag_4^{2+} diffusion coefficient of $D = 10^{-12} m^2 s^{-1}$ as determined from the growth rate fitting, the characteristic collision time is, $\tau_D \approx \frac{l^2}{D} = \frac{(30nm)^2}{10^{-12}\frac{m^2}{s}} \approx 1ms$. This time scale accords with the time range over which the power law scaling of Ag_4^{2+} concentration agrees with the experimental fitted value. This simple scaling estimate emphasizes the importance of the millisecond time scale for reaction-limited nucleation—this time scale accords with the time required for a single collision of two Ag_4^{2+} ions.

The fitted value of $\xi = 0.31$ also compares favorably with an order of magnitude estimate. Assuming a coefficient of $\alpha_{Ag_4^{2+}} \approx 10\,\mu M$ and diffusion-limited aggregation rate constant for reaction (7) of $k \approx 10^{10}\ M^{-1}s^{-1}$ yields a theoretical estimate of $\xi \approx 1$. Taken together, the agreement between experimental and kinetic simulation power law fitting parameters for Ag_4^{2+} clusters at the millisecond time scale, the agreement of the millisecond time scale with the collision time of Ag_4^{2+} clusters, and the agreement of the fitting parameters with diffusion-limited aggregation kinetics provides strong corroborating evidence that nucleation here is reaction limited by aggregation of transient populations of Ag_4^{2+} ions.

2.4. Reconstructing the Reaction Pathway of Intermediate Species

After identifying Ag_4^{2+} as the intermediate species driving radiolytic Ag-cluster nucleation and Ag_4 and Ag^- as the intermediate species mediating nanoparticle growth, we aimed to elucidate the chemical pathways of their formation and decay. The simulations determine the time-dependent concentrations of 49 species participating in 200 coupled chemical reactions. Simply inspecting the competing reactions and concentration transients does not allow for unambiguous determination of the dominant chemical

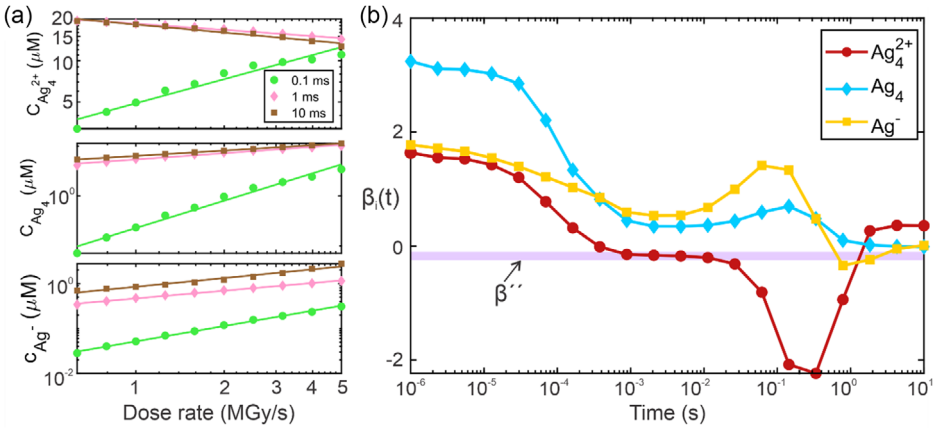

Figure 4. The dose rate dependence of transient silver clusters. a) The concentration of Ag_4^{2+} (top), Ag_4 (middle), and Ag^- (bottom) as a function of dose rate at 0.1 ms (green circle), 1 ms (pink diamond), and 10 ms (brown square) after initiating the reaction. The lines are power law fits to determine $\alpha_i(t)$ and $\beta_i(t)$. b) The dose rate power law scaling exponent of each silver species as a function of simulation time. The purple-shaded region shows the range of power law exponents ($\beta'' = -0.17 \pm 0.07$) determined by fitting the reaction kinetics model (Equation (10)) to the nucleation rate data (cf., Figure 3b).

pathways. Here we open this black box by employing a systematic reaction throughput analysis.

Each reaction, u, contributes to product generation with a specific, time-dependent generation rate, $\mathscr{R}_u(t)$, which depends on the rate constant, k_u, and reactant concentrations, c_v, at time t:

$$\mathscr{R}_u(t) = k_u \prod_v c_v(t) \tag{11}$$

Such a reaction-specific generation rate must not be confused with the generation rate of a single chemical species in a reaction network ($R_i(t) = \sum_u k_u \prod_v c_v(t)$). The latter originates from the sum of all generation/consumption rates for a given species, i (see the first two terms of Equation (16) in the Experimental Section). Consequently, Equation (11) allows for determining the flux of material through a single reaction if the time-dependent concentration of the reactants is known. This enables quantifying the role of single reactions in controlling the transient concentration of species in a large reaction network.

To illustrate this approach, we apply Equation (11) to all the reactions involving silver species (Table S1, Supporting Information). An example is shown for 1 MGy s^{-1} in **Figure 5**. Supporting Movie 1, Supporting Information shows a movie of the reaction throughput graphic for all dose rates tested. At early reaction times up to about 1 ms, Ag^+ reacts with aggressive primary radiolysis products ($H^{\cdot}$, $OH^{\cdot}$, e_h^-), forming AgH^+, $AgOH^+$, and Ag (purple-shaded reactions in Figure 5). Notably, $AgOH^+$ throughput is less pronounced, which is in line with the order of magnitude slower rate constant and the presence of *tert*-butanol as an $OH^{\cdot}$ radical scavenger. Furthermore, O_3-mediated oxidation (dark blue shaded) yielding AgO^+ exhibits negligible throughput as the rate constants are relatively small, and radiolytic O_3 formation does not play a major role during LPTEM.[75]

AgH^+ disproportionation into H^+ and Ag occurs after the initial buildup of AgH^+, leading to a low and nearly constant steady-state concentration after 10 ms. Simultaneously, $AgOH^+$ reacts with protons over time scales of 0.1–1 ms to form Ag^{2+} and OH^-. This is an equilibrium reaction with a fast forward rate constant and slow backward constant, which leads to a very low concentration of $AgOH^+$ in the system (turquoise-shaded reactions). Consequently, the oxidizing reaction cascade species are of minor importance for the subsequent reaction cascade

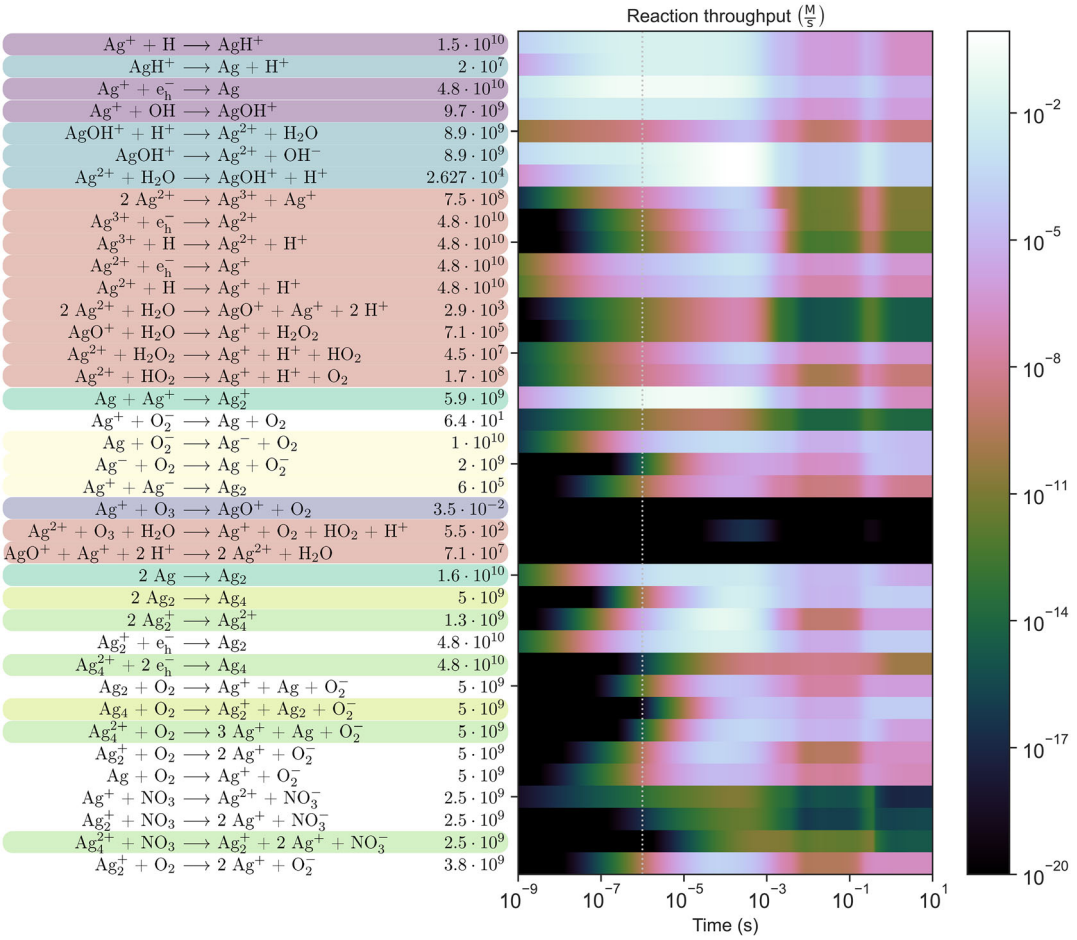

Figure 5. Reaction-specific generation rate analysis for all simulated Ag-containing species at a dose rate of 1 MGy s^{-1}. The rate constants of each reaction are given to their right with units of $M^{-(n-1)}$ s^{-1}, with n as reaction order. The reaction shading color denotes specific reaction pathways discussed in the main text. The color plot on the right shows the reaction throughput calculated using Equation (11). The dotted line denotes 1 µs, the time after which homogeneous kinetics take over. The corresponding time dependent species concentrations are shown in Figure 1.

(red). AgH^+ disproportionation into Ag and H^+ paves the way for Ag_2^+ formation *via* reaction of Ag and Ag^+, which is the dominant reaction in the µs regime along with Ag_2 formation *via* bimolecular Ag reactions (dark green shading). The higher Ag^+ concentration, however, favors formation of Ag_2^+, which lays the pathway for transient accumulation of Ag_4^{2+} at millisecond time scales. The generation of Ag_4^{2+} ions only occurs *via* a single reaction:

$$2\,Ag_2^+ \xrightarrow{1.3\cdot10^9\,\frac{1}{M\,s}} Ag_4^{2+} \quad (12)$$

However, the decay of the ion is divided among three reactions (13)–(15), which are as follows (see Table S1, Supporting Information):

$$Ag_4^{2+} + 2e_h^- \xrightarrow{4.8\cdot10^{10}\,\frac{1}{M^2\,s}} Ag_4 \quad (13)$$

$$Ag_4^{2+} + O_2 \xrightarrow{5\cdot10^9\,\frac{1}{M\,s}} 3Ag^+ + Ag + O_2^- \quad (14)$$

$$Ag_4^{2+} + NO_3 \xrightarrow{2.5\cdot10^9\,\frac{1}{M\,s}} Ag_2^+ + 2Ag^+ + NO_3^- \quad (15)$$

Following the simulated concentration evolution (Figure 1a) shows that Ag_4 concentration increases while Ag_4^{2+} decreases after ≈100 ms, suggesting direct reduction of Ag_4^{2+} by hydrated electrons is the dominant reduction pathway (reaction (13)). The rate throughput analysis demonstrates otherwise. Calculating the reaction-specific generation rate using Equation (11) reveals that the oxidative disproportionation of Ag_4^{2+} by O_2 (reaction (14)) is the dominant decay process, exceeding the reduction reaction rate by orders of magnitude (**Figure 6**). Oxidation by the nitrate radical (reaction (15)) is of minor impact under the regarded conditions. After about 1 s, reactions (12) and (14) compensate each other while maintaining a high activity, leading to the steady state. Hence, the approach illustrates the dynamic nature of the steady state, in which forward and backward processes compensate for each other.

As the Ag_4^{2+} concentration decays, Ag_4 and Ag^- rise in concentration. Ag_4 is built up by reaction (13) and aggregation of Ag_2 dimers, which is balanced by an oxidative decay (see Table S1, Supporting Information and yellow-green shaded reactions in Figure 5):

$$2Ag_2 \xrightarrow{5\cdot10^9\,\frac{1}{M\,s}} Ag_4 \quad (16)$$

$$Ag_4 + O_2 \xrightarrow{5\cdot10^9\,\frac{1}{M\,s}} Ag_2^+ + 2Ag_2 + O_2^- \quad (17)$$

Reaction throughput analysis confirms that Ag_4 is indeed mainly formed by reaction (16) instead of direct Ag_4^{2+} reduction (reaction (13)) (Figure 6b). At steady state, dimer attachment and oxidation balance each other. In turn, Ag^- can be formed *via* Ag reduction by radiolytically formed O_2^- and decays *via* either oxidation or Ag^+ attachment:[84,87]

$$Ag + O_2^- \xrightarrow{1\cdot10^{10}\,\frac{1}{M\,s}} Ag^- + O_2 \quad (18)$$

$$Ag^- + O_2 \xrightarrow{2\cdot10^9\,\frac{1}{M\,s}} Ag + O_2^- \quad (19)$$

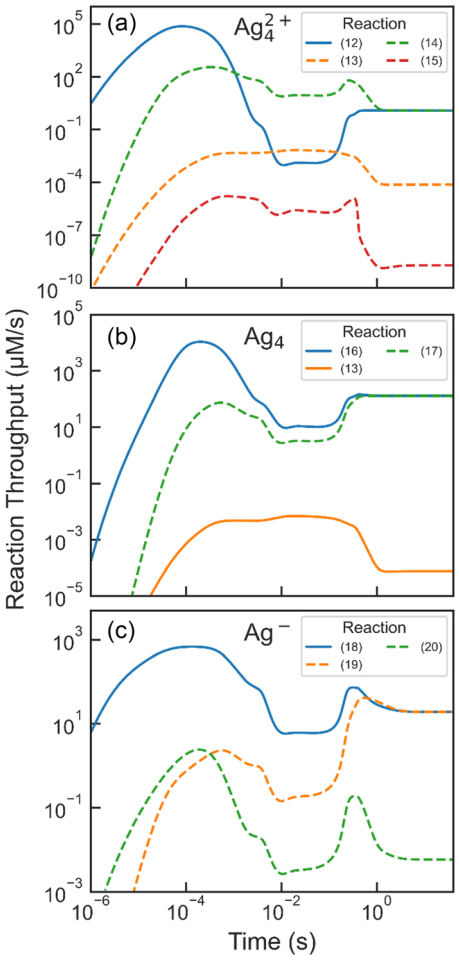

Figure 6. Reaction-specific generation rates (Equation (11)) at a dose rate of 1 MGy s^{-1} for all reactions that incorporate a) Ag_4^{2+}, b) Ag_4, and c) Ag^- either as reactant (dashed) or product (solid).

$$Ag^+ + Ag^- \xrightarrow{6\cdot10^5\,\frac{1}{M\,s}} Ag_2 \quad (20)$$

Figure 6c shows the corresponding reaction throughput analysis, which corresponds to the yellow shading in Figure 5. Reactions (18) and (19) reach steady state after times of a few seconds. Notably, reaction (20) dominates Ag^- decay at short time scales of 10^{-5}–10^{-3} s, despite its comparably sluggish reaction rate. Prior work showed that this mechanism accelerates the reduction of Ag^+ in the presence of silver nanoparticles containing Ag^- on their surface.[87] This is due to the relatively high Ag^+ precursor concentration and illustrates once more that reaction rate constants alone can cause misinterpretations of reaction network interplay.

Moreover, rate throughput analysis in combination with graph theory allows for simultaneous illustration of concentration and reaction pathway evolution. An exemplary graph of the full reaction network at 1.3 ms after irradiation with 1 MGy s^{-1} is plotted in Figure S4, Supporting Information. The full transient evolution is shown in Supporting Movie 2, Supporting Information. In contrast to previous, concentration-independent graph

visualizations of radiation chemistry networks,[50,75,76] the node size corresponds to the concentration of the species and the lines display the reaction-specific generation rate. This provides a holistic overview of the activity of the entire network.

This work describes the formation mechanism of silver nanoparticles under electron irradiation during LPTEM experiments, which is expected to differ in some ways from bulk solution chemical synthesis. In the latter, a chemical reducing agent is utilized to establish a predominantly reducing chemical environment, while radiolysis introduces both oxidizing and reducing species. Differences in precursor reduction reaction order and kinetics are expected when comparing LPTEM synthesis and solution chemistry.[43] However, prior work by Wang et al.[32] and Aliyah et al.[98] demonstrated that the growth mechanism and characteristics (size, shape, composition) of metal nanoparticles synthesized by each method are similar when using low magnification dose rate-controlled STEM imaging as in this study. One important anticipated difference for silver nanoparticle synthesis by solution chemistry is the absence of superoxide radicals. The reaction throughput analysis shows these species are responsible for formation of silver anions (reaction (18)), which are therefore not expected to exist during solution chemical synthesis. Instead, the reaction network suggests the predominant species will be zero-valent silver monomers and clusters as well as silver cations, which form *via* reaction between silver monomers and silver ions. Note, however, that superoxide forms under UV exposure to nanosilver suspensions,[84,87] which is relevant for environmental conditions and photocatalysis.[87,99,100] Silver cations like Ag_4^{2+} are still expected to form transiently due to rapid depletion of silver ions during conventional synthesis. Taken together, this analysis suggests reaction throughput analysis as a powerful approach to extrapolate detailed chemical pathways from radiation synthesis to traditional solution chemistry.

3. Conclusion

In conclusion, we applied reaction kinetic simulations to interpret experimental LPTEM observations of radiolytic-induced silver nanoparticle nucleation and growth. Kinetic simulations provided silver species concentration as a function of time and dose rate, while LPTEM experiments quantified the silver nanoparticle growth and nucleation rates. The simulated steady-state concentration of silver species as a function of dose rate is well described by a power law function, which enabled expressing nucleation and growth rate models in terms of dose rate, the independent variable in the LPTEM experiments. We used data fitting to test these models against the experimentally measured nucleation and growth rates. For nanoparticle growth, we tested the LSW model for diffusion-limited growth against the growth rate data and found the model was consistent with Ag_4 and Ag^- as the dominant intermediate species. As these species also had the highest concentration across all dose rates, the analysis strongly suggests these are the key intermediate species attaching to growing nanoparticles.

We used a similar approach to evaluate if Ag nanoparticle nucleation could be described by CNT. Fitting the experimental nucleation rate data with CNT yielded unrealistic material constants and power law dependence on concentration inconsistent with any of the species in the reaction simulations. These inconsistencies ruled out CNT for describing silver nanoparticle nucleation. Instead, we proposed a reaction limit nucleation mechanism that assumed silver cluster aggregation is the rate limit step for particle nucleation. However, again the power law coefficients for silver concentration were inconsistent with any of the steady-state concentrations of silver species. Instead, we found that transient concentrations of Ag_4^{2+} at millisecond time scales were consistent with the reaction-limited nucleation model. Scaling analyses showed that the characteristic time scale for Ag_4^{2+} ion collision was on the order of milliseconds, further supporting this mechanism. Finally, we developed a reaction throughput analysis to demonstrate the reaction pathway for formation of transient populations of Ag_4^{2+} ions and large steady-state concentrations of Ag_4 and Ag^-. Overall, the results of the reaction throughput analysis uncovered the underlying chemical pathway leading to the nonclassical nucleation pathway described above. Correlative simulation and LPTEM measurements thus lay the foundation for quantitative LPTEM to uncover so far unknown nucleation and growth mechanisms relevant to nanostructure synthesis and design. We expect this approach will find broad usage in identifying nucleation and growth mechanisms of nanoparticles that are known to form by cluster aggregation mechanisms and intermediate clusters, such as quantum dots[101] and metal nanoparticles with strongly binding ligands.[102]

4. Experimental Section

LPTEM Experiments: The silver synthesis exploits electron beam-induced water radiolysis, forming reductive species such as hydrated electrons (e_h^-) (the related generation values are listed in Table S2, Supporting Information):[44]

$$H_2O \xrightarrow{\text{irradiation}} H,\ OH,\ H^+,\ OH^-,\ HO_2,\ H_2,\ H_2O_2,\ e_h^- \quad (21)$$

These primary products subsequently react with the solutes, triggering the reaction network listed in Table S1, Supporting Information, and can yield silver reduction. We utilized the LPTEM dataset from Wang et al.[56] which measured the number and sizes of silver nanoparticles forming under continuous STEM imaging of a 0.1 mM silver nitrate aqueous solution containing 100 mM *tert*-butanol as a hydroxyl radical scavenger. The presence of silver nanoparticles was supported by HRTEM.[56] The dose rate of the experiment was varied by modifying the STEM probe beam current at a constant magnification of 100 000×. A single particle tracking image analysis algorithm was utilized to extract the growth trajectory of hundreds of particles per dose rate. The average growth rate was measured at each dose rate by fitting a line to each particle growth trajectory and then averaging the slope of each line, the growth rate, over several hundred particles. The average growth rate and average particle size were determined from in situ movies of nanoparticle growth measuring the evolution of the particles' projected areas combined with multitarget particle tracking (Figure S3, Supporting Information). The growth rate of a nanoparticle was measured by fitting a line to the first 30 s of each individual particle growth trajectory and then averaging all the growth rates together for a single dose rate. The particle size in Equation (4) was taken as the average size of each particle over the growth rate fitting time range. The nucleation rate at each dose rate was taken as the total number of particles divided by the total time of the LPTEM movie and the image area. This method was chosen due to the nonconstant nucleation rate throughout each dataset (Figure S3, Supporting Information). The dose rate was

varied in three steps between about 0.9 and 5 MGy s^{-1} and nucleation and growth rate measurements were obtained from at least two in situ movies at each dose rate.

Silver Nitrate Radiolysis Simulations: The radiation chemistry of silver nitrate (0.1 mM) and *tert*-butanol (100 mM) in degassed water was estimated by using a kinetic model balancing 201 reactions and 49 reactants *via* numerical solution of coupled ordinary differential equations:

$$\frac{dc_i}{dt} = \sum_j k_j \left(\prod_l c_l \right) - \sum_{m \neq j} k_m \left(\prod_n c_n \right) + \rho \dot{d} G_i \quad (22)$$

Here, the temporal change in concentration of a species i, $\frac{dc_i}{dt}$, was calculated using the rate constants k and concentrations c of all reactants that yield i as a product (first term), or where i is serving as reactant (second term). To account for electron beam effects, the third term incorporates the generation value (G-value) G_i of i and the density of water ($\rho = 1\,g\,L^{-1}$). G_i is nonzero if i is a primary radiolysis product or H_2O (see Table S2, Supporting Information for details). This zero-dimensional simulation models a perfectly mixed solution. Thus, diffusion and effects of the scanning electron beam were neglected.[44,103] Simulations were conducted using AuRaCh, a tool for Automated Radiation Chemistry simulations.[50] The reactions and kinetics in the model are listed in Table S1, Supporting Information and the G-values in Table S2, Supporting Information. The AuRaCh-ready reaction file is available at https://github.com/BirkFritsch/Radiolysis-simulations.

Supporting Information

Supporting Information is available from the Wiley Online Library or from the author.

Acknowledgements

J.S. and B.F. contributed equally to this work. The authors thank Sz-Chian Liou for assistance with TEM operation and Jim De Yoreo for useful discussions on the nucleation mechanism. This material is based upon work supported by the National Science Foundation under grant no. 2045258. Financial support by the German Research Foundation (DFG) via the Cluster of Excellence "Engineering of Advanced Materials (EAM)" (53244630) is gratefully acknowledged.

Open Access funding enabled and organized by Projekt DEAL.

Conflict of Interest

The authors declare no conflict of interest.

Author Contributions

Jiayue Sun: Methodology, validation, writing—review and editing, writing—original draft, visualization. **Birk Fritsch**: Formal analysis, methodology, software, validation, writing—review and editing, writing—original draft, visualization, supervision, conceptualization. **Andreas Körner**: Methodology, formal analysis, validation, writing—review and editing. **Mehran Taherkhani**: Methodology, validation, writing—review and editing. **Mei Wang**: Methodology, investigation, validation, formal analysis, visualization. **Chiwoo Park**: Methodology, software, data curation. **Andreas Hutzler**: Conceptualization, methodology, formal analysis, validation, visualization, resources, writing—review and editing, writing—original draft, visualization, supervision, funding acquisition. **Taylor J. Woehl**: Conceptualization, methodology, software, validation, formal analysis, resources, writing—review and editing, writing—original draft, visualization, supervision, funding acquisition.

Data Availability Statement

The data that support the findings of this study are available from the corresponding author upon reasonable request.

Keywords

aggregation, liquid phase electron microscopy, nonclassical growth, radiolysis, silver nanoparticles

Received: March 29, 2024
Revised: June 28, 2024
Published online:

[1] W. Li, K. Li, Y. Ye, S. Zhang, Y. Liu, G. Wang, C. Liang, H. Zhang, H. Zhao, *Commun. Chem.* **2021**, *4*, 10.
[2] Y. Li, H. Li, Y. Zhao, D. Ji, P. Guo, G. Li, X. Zhao, *Small* **2023**, *19*, 2303065.
[3] G. Li, G. Han, L. Wang, X. Cui, N. K. Moehring, P. R. Kidambi, D. Jiang, Y. Sun, *Nat. Commun.* **2023**, *14*, 525.
[4] M.-Q. He, Y. Ai, W. Hu, L. Guan, M. Ding, Q. Liang, *Adv. Mater.* **2023**, *35*, 2211915.
[5] M. Wuithschick, A. Birnbaum, S. Witte, M. Sztucki, U. Vainio, N. Pinna, K. Rademann, F. Emmerling, R. Kraehnert, J. Polte, *ACS Nano* **2015**, *9*, 7052.
[6] L. Qiao, N. Pollard, R. D. Senanayake, Z. Yang, M. Kim, A. S. Ali, M. T. Hoang, N. Yao, Y. Han, R. Hernandez, A. Z. Clayborne, M. R. Jones, *Nat. Commun.* **2023**, *14*, 4408.
[7] B. Jin, Y. Wang, Z. Liu, A. France-Lanord, J. C. Grossman, C. Jin, R. Tang, *Adv. Mater.* **2019**, *31*, 1808225.
[8] N. T. K. Thanh, N. Maclean, S. Mahiddine, *Chem. Rev.* **2014**, *114*, 7610.
[9] V. K. LaMer, R. H. Dinegar, *J. Am. Chem. Soc.* **1950**, *72*, 4847.
[10] J. van Embden, J. E. Sader, M. Davidson, P. Mulvaney, *J. Phys. Chem. C* **2009**, *113*, 16342.
[11] D. T. Robb, V. Privman, *Langmuir* **2008**, *24*, 26.
[12] Y.-S. Jun, Y. Zhu, Y. Wang, D. Ghim, X. Wu, D. Kim, H. Jung, *Annu. Rev. Phys. Chem.* **2022**, *73*, 453.
[13] T. Sugimoto, *J. Colloid Interface Sci.* **2007**, *309*, 106.
[14] T. Sugimoto, *Adv. Colloid Interface Sci.* **1987**, *28*, 65.
[15] J. J. De Yoreo, P. U. P. A. Gilbert, N. A. J. M. Sommerdijk, R. L. Penn, S. Whitelam, D. Joester, H. Zhang, J. D. Rimer, A. Navrotsky, J. F. Banfield, A. F. Wallace, F. M. Michel, F. C. Meldrum, H. Cölfen, P. M. Dove, *Science* **2015**, *349*, aaa6760.
[16] M. A. Watzky, R. G. Finke, *Chem. Mater.* **1997**, *9*, 3083.
[17] M. A. Watzky, R. G. Finke, *J. Am. Chem. Soc.* **1997**, *119*, 10382.
[18] S. Mozaffari, W. Li, C. Thompson, S. Ivanov, S. Seifert, B. Lee, L. Kovarik, A. M. Karim, *Nanoscale* **2017**, *9*, 13772.
[19] B. Jin, Y. Wang, C. Jin, J. J. De Yoreo, R. Tang, *J. Phys. Chem. Lett.* **2021**, *12*, 5938.
[20] A. Loiudice, R. Buonsanti, *Nat. Synth.* **2022**, *1*, 344.
[21] N. D. Loh, S. Sen, M. Bosman, S. F. Tan, J. Zhong, C. A. Nijhuis, P. Král, P. Matsudaira, U. Mirsaidov, *Nat. Chem.* **2017**, *9*, 77.
[22] D. Li, M. H. Nielsen, J. R. I. Lee, C. Frandsen, J. F. Banfield, J. J. De Yoreo, *Science* **2012**, *336*, 1014.
[23] C. Zhu, S. Liang, E. Song, Y. Zhou, W. Wang, F. Shan, Y. Shi, C. Hao, K. Yin, T. Zhang, J. Liu, H. Zheng, L. Sun, *Nat. Commun.* **2018**, *9*, 421.
[24] J. F. Banfield, S. A. Welch, H. Zhang, T. T. Ebert, R. L. Penn, *Science* **2000**, *289*, 751.
[25] T. J. Woehl, C. Park, J. E. Evans, I. Arslan, W. D. Ristenpart, N. D. Browning, *Nano Lett.* **2014**, *14*, 373.

[26] F. Wang, V. N. Richards, S. P. Shields, W. E. Buhro, *Chem. Mater.* **2014**, *26*, 5.
[27] M. Wuithschick, S. Witte, F. Kettemann, K. Rademann, J. Polte, *Phys. Chem. Chem. Phys.* **2015**, *17*, 19895.
[28] W. Dachraoui, M. I. Bodnarchuk, R. Erni, *ACS Nano* **2022**, *16*, 14198.
[29] R. Xie, Z. Li, X. Peng, *J. Am. Chem. Soc.* **2009**, *131*, 15457.
[30] M. A. Wall, B. M. Cossairt, J. T. C. Liu, *J. Phys. Chem. C* **2018**, *122*, 9671.
[31] W. Li, M. G. Taylor, D. Bayerl, S. Mozaffari, M. Dixit, S. Ivanov, S. Seifert, B. Lee, N. Shanaiah, Y. Lu, L. Kovarik, G. Mpourmpakis, A. M. Karim, *Nanoscale* **2021**, *13*, 206.
[32] M. Wang, A. Leff, Y. Li, T. Woehl, *ACS Nano* **2021**, *15*, 2578.
[33] J. J. Calvin, A. S. Brewer, A. P. Alivisatos, *Nat. Synth.* **2022**, *1*, 127.
[34] A. Heuer-Jungemann, N. Feliu, I. Bakaimi, M. Hamaly, A. Alkilany, I. Chakraborty, A. Masood, M. F. Casula, A. Kostopoulou, E. Oh, K. Susumu, M. H. Stewart, I. L. Medintz, E. Stratakis, W. J. Parak, A. G. Kanaras, *Chem. Rev.* **2019**, *119*, 4819.
[35] T. S. Rodrigues, M. Zhao, T.-H. Yang, K. D. Gilroy, A. G. M. da Silva, P. H. C. Camargo, Y. Xia, *Chem. Eur. J.* **2018**, *24*, 16944.
[36] H. Zheng, R. K. Smith, Y. Jun, C. Kisielowski, U. Dahmen, A. P. Alivisatos, *Science* **2009**, *324*, 1309.
[37] J. Sun, A. Leff, Y. Li, T. J. Woehl, *Nanoscale* **2023**, *15*, 10447.
[38] T. J. Woehl, J. E. Evans, I. Arslan, W. D. Ristenpart, N. D. Browning, *ACS Nano* **2012**, *6*, 8599.
[39] T. R. Henninen, D. Keller, R. Erni, *ChemNanoMat* **2021**, *7*, 110.
[40] W. Dachraoui, T. R. Henninen, D. Keller, R. Erni, *Sci. Rep.* **2021**, *11*, 23965.
[41] Y. Son, B. H. Kim, B. K. Choi, Z. Luo, J. Kim, G.-H. Kim, S.-J. Park, T. Hyeon, S. Mehraeen, J. Park, *ACS Appl. Mater. Interfaces* **2022**, *14*, 22810.
[42] T. Woehl, P. Abellan, *J. Microsc.* **2017**, *265*, 135.
[43] T. J. Woehl, *Chem. Mater.* **2020**, *32*, 7569.
[44] N. M. Schneider, M. M. Norton, B. J. Mendel, J. M. Grogan, F. M. Ross, H. H. Bau, *J. Phys. Chem. C* **2014**, *118*, 22373.
[45] J. M. Yuk, J. Park, P. Ercius, K. Kim, D. J. Hellebusch, M. F. Crommie, J. Y. Lee, A. Zettl, A. P. Alivisatos, *Science* **2012**, *336*, 61.
[46] H. Wang, K. H. Nagamanasa, Y.-J. Kim, O.-H. Kwon, S. Granick, *ACS Nano* **2018**, *12*, 8572.
[47] M. R. Hauwiller, J. C. Ondry, C. M. Chan, P. Khandekar, J. Yu, A. P. Alivisatos, *J. Am. Chem. Soc.* **2019**, *141*, 4428.
[48] I. A. Moreno-Hernandez, M. F. Crook, J. C. Ondry, A. P. Alivisatos, *J. Am. Chem. Soc.* **2021**, *143*, 12082.
[49] F. M. Ross, *Science* **2015**, *350*, aaa9886.
[50] B. Fritsch, T. S. Zech, M. P. Bruns, A. Körner, S. Khadivianazar, M. Wu, N. Zargar Talebi, S. Virtanen, T. Unruh, M. P. M. Jank, E. Spiecker, A. Hutzler, *Adv. Sci.* **2022**, *9*, 2202803.
[51] B. L. Mehdi, A. Stevens, L. Kovarik, N. Jiang, H. Mehta, A. Liyu, S. Reehl, B. Stanfill, L. Luzi, W. Hao, L. Bramer, N. D. Browning, *Appl. Phys. Lett.* **2019**, *115*, 063102.
[52] S. Merkens, G. De Salvo, A. Chuvilin, *Nano Express* **2023**, *3*, 045006.
[53] D. Alloyeau, W. Dachraoui, Y. Javed, H. Belkahla, G. Wang, H. Lecoq, S. Ammar, O. Ersen, A. Wisnet, F. Gazeau, C. Ricolleau, *Nano Lett.* **2015**, *15*, 2574.
[54] J. H. Park, N. M. Schneider, J. M. Grogan, M. C. Reuter, H. H. Bau, S. Kodambaka, F. M. Ross, *Nano Lett.* **2015**, *15*, 5314.
[55] S. A. Canepa, B. T. Sneed, H. Sun, R. R. Unocic, K. Mølhave, *J. Phys. Chem. C* **2018**, *122*, 2350.
[56] M. Wang, C. Park, T. J. Woehl, *Chem. Mater.* **2018**, *30*, 7727.
[57] M. Wang, T. Dissanayake, C. Park, K. Gaskell, T. Woehl, *J. Am. Chem. Soc.* **2019**, *141*, 13516.
[58] A. Khelfa, J. Nelayah, H. Amara, G. Wang, C. Ricolleau, D. Alloyeau, *Adv. Mater.* **2021**, *33*, 2102514.
[59] S. Lee, N. M. Schneider, S. F. Tan, F. M. Ross, *ACS Nano* **2023**, *17*, 5609.
[60] K. L. Jungjohann, S. Bliznakov, P. W. Sutter, E. A. Stach, E. A. Sutter, *Nano Lett.* **2013**, *13*, 2964.
[61] D. J. Kelly, M. Zhou, N. Clark, M. J. Hamer, E. A. Lewis, A. M. Rakowski, S. J. Haigh, R. V. Gorbachev, *Nano Lett.* **2018**, *18*, 1168.
[62] C. Wang, Q. Qiao, T. Shokuhfar, R. F. Klie, *Adv. Mater.* **2014**, *26*, 3410.
[63] R. Tausch-Treml, A. Henglein, J. Lilie, *Ber. Bunsenges. Phys. Chem.* **1978**, *82*, 1335.
[64] B. G. Ershov, E. Janata, A. Henglein, A. Fojtik, *J. Phys. Chem.* **1993**, *97*, 4589.
[65] J. Belloni, M. Mostafavi, H. Remita, J.-L. Marignier, M.-O. Delcourt, *New J. Chem.* **1998**, *22*, 1239.
[66] M. Mostafavi, G. R. Dey, L. François, J. Belloni, *J. Phys. Chem. A* **2002**, *106*, 10184.
[67] T. Woehl, T. Moser, J. Evans, F. Ross, *MRS Bull.* **2020**, *45*, 746.
[68] A. Ahmed, E. C. Boyle, P. A. Kottke, A. G. Fedorov, *Sci. Adv.* **2021**, *7*, eabj8751.
[69] B. Ambrožič, A. Prašnikar, N. Hodnik, N. Kostevšek, B. Likozar, K. Ž. Rožman, S. Šturm, *Chem. Sci.* **2019**, *10*, 8735.
[70] G. R. Dey, C. R. McCormick, S. S. Soliman, A. J. Darling, R. E. Schaak, *ACS Nano* **2023**, *17*, 5943.
[71] C. Sun, Y. Jiang, L. Zhang, K. Wei, M. Yuan, *ACS Nano* **2023**, *17*, 17600.
[72] J. Bang, I. K. Moon, Y.-K. Kim, J. Oh, *Small Struct.* **2023**, *4*, 2200283.
[73] J. Korpanty, L. R. Parent, N. C. Gianneschi, *Nano Lett.* **2021**, *21*, 1141.
[74] J. Korpanty, K. Gnanasekaran, C. Venkatramani, N. Zang, N. C. Gianneschi, *Cell Rep. Phys. Sci.* **2022**, *3*, 100772.
[75] B. Fritsch, P. Malgaretti, J. Harting, K. J. J. Mayrhofer, A. Hutzler, *Precis. Chem.* **2023**, *1*, 592.
[76] B. Fritsch, A. Körner, T. Couasnon, R. Blukis, M. Taherkhani, L. G. Benning, M. P. M. Jank, E. Spiecker, A. Hutzler, *J. Phys. Chem. Lett.* **2023**, *14*, 4644.
[77] G. Buxton, S. Robin, in *Compilation of Rate Constants for the Reactions of Metal Ions in Unusual Valency States*, Government Printing Office, Washington, DC **1978**.
[78] A. Kumar, P. Neta, *J. Phys. Chem.* **1979**, *83*, 3091.
[79] B. G. Ershov, *Russ. Chem. Rev.* **1981**, *50*, 1119.
[80] Y. Katsumura, P. Y. Jiang, R. Nagaishi, T. Oishi, K. Ishigure, Y. Yoshida, *J. Phys. Chem.* **1991**, *95*, 4435.
[81] B. G. Ershov, E. Janata, A. V. Gordeeva, *Russ. Chem. Bull.* **2005**, *54*, 1874.
[82] A. Sarkar, E. Janata, *Z. Phys. Chem.* **2007**, *221*, 403.
[83] B. G. Ershov, P. A. Morozov, A. V. Gordeeev, *Russ. J. Phys. Chem.* **2012**, *86*, 1795.
[84] N. F. Adegboyega, V. K. Sharma, K. M. Siskova, R. Vecerova, M. Kolar, R. Zbořil, J. L. Gardea-Torresdey, *Environ. Sci. Technol.* **2014**, *48*, 3228.
[85] T. Couasnon, B. Fritsch, M. P. M. Jank, R. Blukis, A. Hutzler, L. G. Benning, *Adv. Sci.* **2023**, *10*, 2301904.
[86] M. A. Hill, F. A. Smith, *Radiat. Phys. Chem.* **1994**, *43*, 265.
[87] A. M. Jones, S. Garg, D. He, A. N. Pham, T. D. Waite, *Environ. Sci. Technol.* **2011**, *45*, 1428.
[88] B. H. Kim, K. Shin, S. G. Kwon, Y. Jang, H.-S. Lee, H. Lee, S. W. Jun, J. Lee, S. Y. Han, Y.-H. Yim, D.-H. Kim, T. Hyeon, *J. Am. Chem. Soc.* **2013**, *135*, 2407.
[89] A. Kulesza, R. Mitrić, V. Bonačić-Koutecký, B. Bellina, I. Compagnon, M. Broyer, R. Antoine, P. Dugourd, *Angew. Chem., Int. Ed.* **2011**, *50*, 878.
[90] W. Ostwald, *1. Abhandlung: Übersättigung und Überkaltung* **1897**, *22U*, 289.
[91] C. Wagner, *Ber. Bunsenges. Phys. Chem.* **1961**, *65*, 581.
[92] B. Medasani, Y. H. Park, I. Vasiliev, *Phys. Rev. B* **2007**, *75*, 235436.
[93] A. Verch, M. Pfaff, N. de Jonge, *Langmuir* **2015**, *31*, 6956.

[94] E. R. White, S. B. Singer, V. Augustyn, W. A. Hubbard, M. Mecklenburg, B. Dunn, B. C. Regan, *ACS Nano* **2012**, *6*, 6308.
[95] T. Uematsu, M. Baba, Y. Oshima, T. Tsuda, T. Torimoto, S. Kuwabata, *J. Am. Chem. Soc.* **2014**, *136*, 13789.
[96] M. N. Yesibolati, K. I. Mortensen, H. Sun, A. Brostrøm, S. Tidemand-Lichtenberg, *Nano Lett.* **2020**, *20*, 7108.
[97] V. Jamali, C. Hargus, A. Ben-Moshe, A. Aghazadeh, H. D. Ha, K. K. Mandadapu, A. P. Alivisatos, *Proc. Natl. Acad. Sci. USA* **2021**, *118*, e2017616118.
[98] K. Aliyah, J. Lyu, C. Goldmann, T. Bizien, C. Hamon, D. Alloyeau, D. Constantin, *J. Phys. Chem. Lett.* **2020**, *11*, 2830.
[99] K. Wenderich, G. Mull, *Chem. Rev.* **2016**, *116*, 14587.
[100] D. Hoffmeister, S. Finger, L. Fiedler, T.-C. Ma, A. Körner, M. Zlatar, B. Fritsch, K. W. Bodnar, S. Carl, A. Götz, B. A. Zubiri, J. Will, E. Spiecker, S. Cherevko, A. T. S. Freiberg, K. J. J. Mayrhofer, S. Thiele, A. Hutzler, C. van Pham, *Adv. Sci.* **2024**, *11*, 2402991.
[101] D. C. Gary, M. W. Terban, S. J. L. Billinge, B. M. Cossairt, *Chem. Mater.* **2015**, *27*, 1432.
[102] Y. Negishi, K. Nobusada, T. Tsukuda, *J. Am. Chem. Soc.* **2005**, *127*, 5261.
[103] J. Lee, D. Nicholls, N. D. Browning, B. L. Mehdi, *Phys. Chem. Chem. Phys.* **2021**, *23*, 17766.